

Stochastic Flights of Propellers

Margaret Pan^{1*}, Hanno Rein², Eugene Chiang¹, and Steven N. Evans³

¹*Department of Astronomy, University of California at Berkeley, Hearst Field Annex B-20, Berkeley CA 94720-3411, USA*

²*Institute for Advanced Study, 1 Einstein Drive, Princeton, NJ 08540, USA*

³*Department of Statistics, University of California at Berkeley, 367 Evans Hall, Berkeley CA 94720-3860, USA*

Submitted: 8 March 2013

ABSTRACT

Kilometer-sized moonlets in Saturn’s A ring create S-shaped wakes called “propellers” in surrounding material. The *Cassini* spacecraft has tracked the motions of propellers for several years and finds that they deviate from Keplerian orbits with constant semimajor axes. The inferred orbital migration is known to switch sign. We show using a statistical test that the time series of orbital longitudes of the propeller Blériot is consistent with that of a time-integrated Gaussian random walk. That is, Blériot’s observed migration pattern is consistent with being stochastic. We further show, using a combination of analytic estimates and collisional N -body simulations, that stochastic migration of the right magnitude to explain the *Cassini* observations can be driven by encounters with ring particles 10–20 m in radius. That the local ring mass is concentrated in decameter-sized particles is supported on independent grounds by occultation analyses.

Key words: diffusion – methods: statistical – methods: numerical – planets and satellites: rings – planet-disc interactions – celestial mechanics

1 INTRODUCTION

Propellers are disturbances in Saturn’s rings caused by moonlets 0.1–1 km in radius (Tiscareno et al. 2006). The moonlets gravitationally repel material to either side of their orbits, creating partial gaps that diffuse shut via inter-particle collisions (Spahn & Sremčević 2000; Sremčević et al. 2002; Seiß et al. 2005; Lewis & Stewart 2009). Even with the *Cassini* spacecraft’s resolving power, the moonlets themselves are too small to be detected directly. Their existence and sizes are inferred from the larger S-shaped wakes resembling propellers that they leave behind, on scales of several Hill radii (Seiß et al. 2005; Tiscareno et al. 2010, hereafter T10).

Intriguingly, multi-epoch *Cassini* observations of a number of propellers reveal that propellers deviate from strictly Keplerian orbits: the orbital longitudes λ of a propeller drift away from the values expected for an orbit of fixed semimajor axis (T10). Longitude residuals $\Delta\lambda$ range from 0.01–0.31 degrees over $\Delta t = 1.3$ –4.3 years; see Table 1 of T10. By far the most extensive data exist for the propeller dubbed Blériot, whose longitudes have been measured 89 times at

sporadic intervals over 4.2 years. Blériot’s longitude residuals versus time are shown in Figure 1, reproduced from T10. The measurements of non-Keplerian motion represent the first direct evidence that moons embedded in rings exhibit orbital evolution. Propellers thus provide a test-bed for studying satellite-disk interactions, in particular orbital migration (see, for example, Goldreich & Tremaine 1982).

To establish the order of magnitude of the implied migration, we convert longitude residual $\Delta\lambda$ to the change Δa in the moonlet’s semimajor axis:

$$\Delta a \sim \frac{\Delta\lambda}{\Omega\Delta t} a \sim 30 \left(\frac{\Delta\lambda}{0.1 \text{ deg}} \right) \left(\frac{2 \text{ yr}}{\Delta t} \right) \left(\frac{a}{1.3 \times 10^5 \text{ km}} \right)^{5/2} \text{ m} \quad (1)$$

where Ω is the mean motion (orbital frequency). This inferred radial deviation should not be confused with the azimuthal deviation, which is measured directly from observations to be on the order of $a\Delta\lambda \sim 300$ km. The semimajor axis change Δa observed to date is smaller than the moonlet’s expected physical size.

Two classes of theories have emerged to explain the non-Keplerian motion. In one, propeller-moonlets librate within a resonance established by co-orbital material (Pan & Chiang 2010). In the other, propeller-moonlets are

* e-mail: mpan@astro.berkeley.edu.

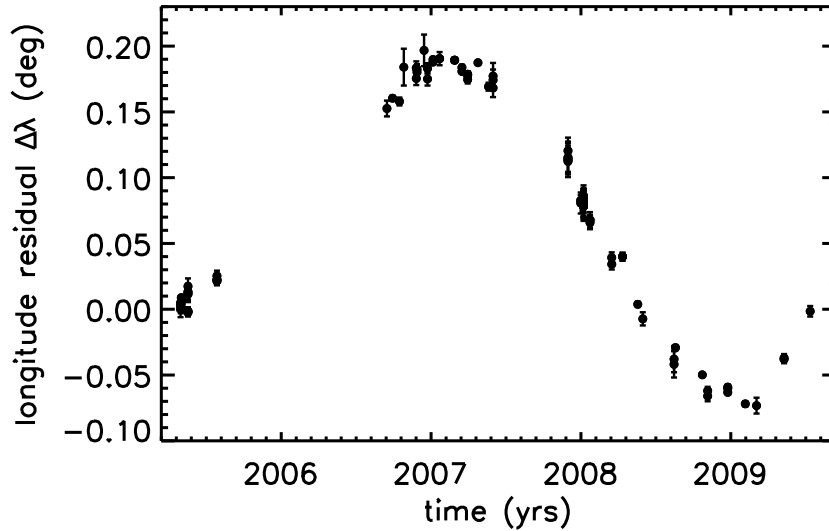


Figure 1. Longitude residuals (deviations from a fixed circular orbit) of the propeller Blériot as seen in 89 *Cassini* images obtained over 4.2 years and as reported by T10. For display purposes, we subtracted a linear trend to place the first and last data points at zero longitude residual.

torqued stochastically by density fluctuations in surrounding ring material (Rein & Papaloizou 2010; Crida et al. 2010). Both types of theories in their current forms are not without problems. Libration amplitudes within the proposed co-orbital resonance damp to zero when account is made of the two-way feedback between the moonlet and the ring (Pan & Chiang 2012). So far, the stochastic migration hypothesis has focused on density fluctuations driven by self-gravity (“self-gravity wakes”; Salo 1995). Rein & Papaloizou (2010) simulated such wakes, and found that they could cause small moonlets, about 25–50 m in radius, to random walk by distances comparable to those cited above. Unfortunately, most propellers, including Blériot, are an order of magnitude larger in size (T10), and thus are not expected to be accelerated significantly by self-gravity wakes. This shortcoming of self-gravity wakes can be remedied by increasing the ring surface density (e.g., Crida et al. 2010), but evidence for such large surface densities is lacking (Colwell et al. 2009).

It may seem surprising that even the most basic issue of whether the non-Keplerian motion is deterministic or random is controversial. A glance at the longitude time series in Figure 1 suggests that Blériot’s motion is smooth or even sinusoidal, with a period of ~ 3.7 yr. Nevertheless, the time series could in fact reflect pure noise. The confusion arises because orbital longitude is a time-integrated quantity:

$$\Delta\lambda = \int^t \Delta\Omega \, dt \quad (2)$$

where $\Delta\Omega$ is the difference between the moonlet’s instantaneous mean motion and that of a fixed reference orbit. The time integration smooths over fluctuations in $\Delta\Omega$; $\Delta\lambda$ is obviously differentiable. The integration also introduces correlations between data points even when $\Delta\Omega$ itself rep-

resents uncorrelated noise: $\Delta\lambda(t)$ depends on the full time history of perturbations up to time t . Both effects conspire to hide any underlying stochasticity.

In this paper, we apply a test, well-known among statisticians but less so among astronomers, that identifies integrated random walks for the special case where the underlying random walk is Gaussian. In effect, the test “undoes” the correlations introduced by the integration to determine whether the integrand $\Delta\Omega$ is consistent with a Gaussian random walk. This test, which we call the “diagonalization test” for reasons explained in §2, is especially useful because it can be applied to data that — as is the case for real-life propellers — are unevenly sampled.¹

The plan of this paper is as follows. In §2, we describe the diagonalization test and apply it to Blériot. We find that Blériot passes the test — that its behavior is consistent with that of an integrated Gaussian random walk. In §3 we describe how such a random walk can be driven by Poisson fluctuations in the encounter rate between large ring particles and a given propeller moonlet (an effect distinct from self-gravity wakes). A summary is given in §4.

¹ If the sampling were uniform, then we could in principle just histogram *second* differences of the sequence of points to check consistency with an integrated Gaussian random walk. Taking differences between adjacent points would produce the Gaussian random walk observed on a uniform grid of times. Taking differences again would produce a sequence of independent, identically distributed Gaussian random variables, with each one being the sum of some common number of the Gaussian steps in the underlying random walk, taken over a set of times disjoint from those leading to the other sums.

2 DIAGONALIZING THE NOISE

We derive and explain the rationale behind the diagonalization test in §2.1, check the test against some case examples in §2.2, and apply the test to Blériot in §2.3.

2.1 Decorrelating the Integrated Gaussian Random Walk

We wish to check if a given time series — for example, the Blériot longitude residuals — is consistent with a time-integrated random walk whose individual steps are independent identically-distributed (IID) Gaussian random variables. We can think of this time-integrated random walk as correlated Gaussian noise in which all the correlations arise from the time integration. If all such correlations were to be eliminated from our given time series, we could then compare what remains to a family of IID Gaussian random variables and thereby test the Gaussian random walk hypothesis. Here we describe one such decorrelation method. The mathematical ideas behind the method are well known (see, for example, Mardia et al. 1979). Indeed, the method overlaps conceptually with recent treatments of pulsar timing noise (Coles et al. 2011).

We first calculate the covariance between any two elements of a time series produced by a time-integrated Gaussian random walk. Although our presentation focuses on the specific case of a time series of orbital longitudes, the underlying algorithm is general. We use Δ for quantities that evolve with time and δ for quantities associated with an individual step in the random walk.

Consider a body whose semimajor axis a undergoes a random walk, taking one step in the walk per timestep. After $n \geq 1$ timesteps of constant length δt , the total change in semimajor axis is

$$\Delta a(n\delta t) = \sum_{j=0}^{n-1} \xi_j \quad (3)$$

where the ξ_j are Gaussian random variables for which $E[\xi_j] = 0$ and $E[\xi_j \xi_k] = (\delta a)^2 \delta_{jk}$. Here E denotes the expected value, and δ_{jk} is the Kronecker delta.

The longitude residual $\Delta\lambda$ is the time integration of $\Delta a \partial\Omega/\partial a$:

$$\Delta\lambda(n\delta t) = - \sum_{i=1}^n \frac{3\Omega}{2a} \Delta a(i\delta t) \delta t \quad (4)$$

$$= - \frac{3\Omega\delta t}{2a} \sum_{i=1}^n \sum_{j=0}^{i-1} \xi_j \quad (5)$$

$$= - \frac{3\Omega\delta t}{2a} \sum_{j=0}^{n-1} (n-j) \xi_j \quad (6)$$

where, as before, δt is the time interval between steps.

The covariance between values of $\Delta\lambda$ after n and m

timesteps, $n < m$, is the expected value of their product:

$$E[\Delta\lambda(n\delta t)\Delta\lambda(m\delta t)] \quad (7)$$

$$= \left(\frac{3\Omega\delta t}{2a}\right)^2 E\left[\left(\sum_{j=0}^{n-1} (n-j)\xi_j\right)\left(\sum_{k=0}^{m-1} (m-k)\xi_k\right)\right] \quad (8)$$

$$= \left(\frac{3\Omega\delta t}{2a}\right)^2 E\left[\sum_{j=0}^{n-1} \xi_j \xi_j (n-j)(m-j)\right] \quad (9)$$

$$= \left(\frac{3\Omega\delta t\delta a}{2a}\right)^2 \sum_{j=0}^{n-1} (n-j)(m-j) \quad (10)$$

$$= \left(\frac{3\Omega\delta t\delta a}{2a}\right)^2 \frac{n}{6}(1-n^2+3m+3nm). \quad (11)$$

Line (9) follows because $\Delta\lambda(n\delta t)$, $\Delta\lambda(m\delta t)$ are two snapshots of the same integrated random walk $\{\Delta\lambda(\delta t), \Delta\lambda(2\delta t), \dots, \Delta\lambda(n\delta t), \dots, \Delta\lambda(m\delta t), \dots\}$. Between timesteps 1 and n , the histories of $\Delta\lambda(n\delta t)$ and $\Delta\lambda(m\delta t)$ coincide exactly — they are 100% correlated — so for summation indices $j, k < n$, in effect $i = j$. After timestep n , the Gaussian variables ξ_n, \dots, ξ_{m-1} contributing to the further history of $\Delta\lambda(m\delta t)$ are completely independent of those that contributed to $\Delta\lambda(n\delta t)$, so the determinants of the motion after timestep n do not contribute to $E[\Delta\lambda(n\delta t)\Delta\lambda(m\delta t)]$.

Given a list of observations at times $\{t_k : 1 \leq k \leq K\}$, and choosing δt to be the characteristic time between changes in semimajor axis, we can use the above with $n = t_k/\delta t$ and $m = t_\ell/\delta t$ to calculate the entries of the corresponding (positive definite, symmetric) covariance matrix $(\Sigma_{k\ell})_{1 \leq k, \ell \leq K}$. If we write $\vec{\Delta\lambda}$ for the column vector with k^{th} entry $\Delta\lambda(t_k)$, then Σ is just the $K \times K$ matrix $E[\vec{\Delta\lambda} \vec{\Delta\lambda}^T]$. By the spectral theorem, there is an orthogonal matrix U and a diagonal matrix Z with positive diagonal entries such that $\Sigma = UZU^T$. To eliminate the correlations in $\Delta\lambda$ due to the time integration, we simply use this covariance matrix to define a suitable linear transformation of the time-series vector $\vec{\Delta\lambda}$:

$$\begin{aligned} &\text{diagonalized (decorrelated) residuals } \vec{r} \\ &= UZ^{-1/2}U^T\vec{\Delta\lambda}, \end{aligned} \quad (12)$$

where $Z^{-1/2}Z^{-1/2} = Z^{-1}$, the inverse of Z . The covariance matrix of such a column vector \vec{r} is

$$E[\vec{r} \vec{r}^T] = UZ^{-1/2}U^T E[\vec{\Delta\lambda} \vec{\Delta\lambda}^T] UZ^{-1/2}U^T \quad (13)$$

$$= UZ^{-1/2}U^T \Sigma UZ^{-1/2}U^T \quad (14)$$

$$= UZ^{-1/2}U^T UZU^T UZ^{-1/2}U^T \quad (15)$$

$$= I, \quad (16)$$

the $K \times K$ identity matrix. Because linear transformations of Gaussian random vectors are also Gaussian (see, for example, Chapter 3 of Mardia et al. 1979), the entries in \vec{r} are IID Gaussian random variables with common expected value 0 and common standard deviation 1 — this fact is effectively the content of Corollary 3.2.1.1 of Mardia et al. (1979).

Note that the covariance matrix Σ is in practice unknown, as only the $\Delta\lambda$ are observed. However, Σ is of the

form $\Sigma = c^2 \tilde{\Sigma}$, where $c = \frac{3\Omega\delta t\delta a}{2a}$ and $\tilde{\Sigma}_{k\ell} = \frac{n}{6}(1 - n^2 + 3m + 3nm)$ with $n = t_k/\delta t$ and $m = t_\ell/\delta t$. The matrix $\tilde{\Sigma}$ is known, but the value of c is unknown (it depends, for example, on the unknown step size δa) and so c must be estimated from data. We do this as follows.

We have $\tilde{\Sigma} = U\tilde{Z}U^T$, where U and $\tilde{Z} = c^{-2}Z$ are readily computed. Set

$$\tilde{r} = U\tilde{Z}^{-1/2}U^T\vec{\Delta\lambda} = c\vec{r}. \quad (17)$$

By the argument above, \tilde{r} is a vector of independent Gaussians with common mean 0 and common standard deviation c . We estimate c using the standard estimator $\hat{c} = \sqrt{\frac{1}{K} \sum_{k=1}^K \tilde{r}_k^2}$. The vector $\hat{c}^{-1}\tilde{r}$ should then be close to \vec{r} when K is not too small and hence should have entries that are approximately Gaussian with common expected value 0 and common standard deviation 1. We can check this by plotting the empirical cumulative distribution function of the entries of $\hat{c}^{-1}\tilde{r}$ against the cumulative distribution function of a Gaussian distribution with expected value 0 and standard deviation 1.

In essence, we have re-expressed the vector of measurements of an integrated Gaussian random walk at the times $\{t_k\}$ in a new basis so that the coefficients with respect to the new basis are independent and identically distributed — hence our term “diagonalization test”. We expect that if the $\{\Delta\lambda(t_k)\}$ arise from a two-fold time integration of individual IID Gaussian kicks, then the entries of $\hat{c}^{-1}\tilde{r} \approx \vec{r}$ will also be distributed as IID Gaussians.

Thus, the diagonalized residuals $\hat{c}^{-1}\tilde{r}$ provide a convenient negative test of whether a time series is consistent with an integrated Gaussian random walk. If the entries of the vector $\hat{c}^{-1}\tilde{r}$ derived from a given observation vector $\vec{\Delta\lambda}$ do not follow a Gaussian distribution reasonably closely, then the time series $\vec{\Delta\lambda}$ cannot result directly from an integrated Gaussian random walk. Conversely, if the entries of $\hat{c}^{-1}\tilde{r}$ are approximately Gaussian, then the observations $\{\Delta\lambda(t_k)\}$ are consistent with (but do not uniquely demand) an integrated Gaussian random walk.

The procedure outlined above is predicated on the assumption that the longitude residuals $\{\Delta\lambda(t_k)\}$ are observed without measurement uncertainty, so that the covariance matrix of the observations is some multiple of $\tilde{\Sigma}$. We will examine the effects of measurement uncertainty in §2.2 and §2.3. The diagonalization procedure also requires that the timestep δt be less than or equal to the time interval between any two of the observation times $\{t_k\}$, so that the columns of $\tilde{\Sigma}$ are independent. We show in §2.3 that any sufficiently small δt that satisfies this condition will result in essentially the same covariance matrix Σ (and hence essentially the same probability model for $\vec{\Delta\lambda}$), provided that δa is modified so that the diffusivity $D = (\delta a)^2/\delta t$ is kept constant. Moreover, we show that any sufficiently small choice of δt will give essentially the same value of $\hat{c}^{-1}\tilde{r}$ and essentially the same diagonalization test. However, for Blériot there is a natural, physically motivated choice of timestep, $\delta t = \Omega^{-1}$ (see §3.1).

Finally, for easy reference we give a short summary of the diagonalization test algorithm:

- (i) The input data required are a time series of values

$\{\Delta\lambda(t_k)\}$ and the corresponding list of times $\{t_k\}$; the goal is to check if the $\{\Delta\lambda(t_k)\}$ are consistent with an integrated Gaussian random walk.

- (ii) Assuming a constant δt smaller than the shortest interval $t_{k+1} - t_k$, use $\tilde{\Sigma}_{k\ell} = \frac{n}{6}(1 - n^2 + 3m + 3nm)$ with $n = t_k/\delta t$ and $m = t_\ell/\delta t$ to compute the matrix $\tilde{\Sigma}$.

- (iii) Compute U and \tilde{Z} from $\tilde{\Sigma} = U\tilde{Z}U^T$ using standard matrix decomposition procedures.

- (iv) Compute \tilde{r} from U , \tilde{Z} , and the $\{\Delta\lambda\}$ using Eq. 17.

- (v) Estimate c using $\hat{c} = \sqrt{\frac{1}{K} \sum_{k=1}^K \tilde{r}_k^2}$, and check that the distribution of $\hat{c}^{-1}\tilde{r}$ has a Gaussian shape and a standard deviation of about 1.

A simple Mathematica implementation of the diagonalization test is available in an online supplement to this paper.

2.2 Gaussian Walks vs. Lévy Flights

As a simple check of the diagonalization test, we apply it to a simulated integrated Gaussian random walk.² The parameters of our simulation are motivated by Blériot. We take the time interval between steps to be $\delta t = \Omega^{-1} \simeq 8842$ s and integrate the walk for 4.3 years. Semimajor axis changes, or “kicks” δa to the moonlet, are generated as Gaussian random variables with standard deviation 1 m. We time-integrate $\delta a(t)$ once to get the cumulative semimajor axis evolution $\Delta a(t)$, and twice to get the associated longitude variations $\Delta\lambda(t)$. The simulated longitudes are then sampled at the times of the Blériot observations. When the Blériot data are appropriately binned (see §2.3), there are 41 observation times.

Figure 2 shows the results of the diagonalization test when applied to our simulated time series containing 41 points. The diagonalized residuals $\hat{c}^{-1}\{\tilde{r}_k\}$ appear close to Gaussian. In our calculation of \hat{c} we dropped 4 extreme values among the $\{\tilde{r}_k\}$ because including these outliers skewed \hat{c} so as to be clearly inconsistent with the vast majority of the $\{\tilde{r}_k\}$. Aside from these few outliers, which actually fall outside the range of the right-hand panel in Figure 2, the agreement with a Gaussian is satisfactory. We find $\hat{c} \simeq 1.2c$ where c is computed using the input parameters of the simulated random walk, which we also consider satisfactory agreement.

To better calibrate what we mean by “satisfactory,” we also apply the diagonalization test to data that does not derive from an integrated Gaussian random walk. We generate instead a time-integrated Lévy flight, where the steps in the underlying random walk are drawn from a power law. Specifically, we assume that the probability of getting a kick of size δa or larger scales as $|\delta a|^{-2/5}$. This power law distribution describes kicks excited by perturbers that are sparsely distributed over an annulus much wider than the moonlet’s Hill sphere radius (see, for example, Collins & Sari 2006, and references therein). Just as in the Gaussian experiment above, we time-integrate the kicks twice to get the associated longitude variations, and we sample the longitudes at the 41

² The simulations described here in §2 should not be confused with the 3D shearing box simulations of §3.

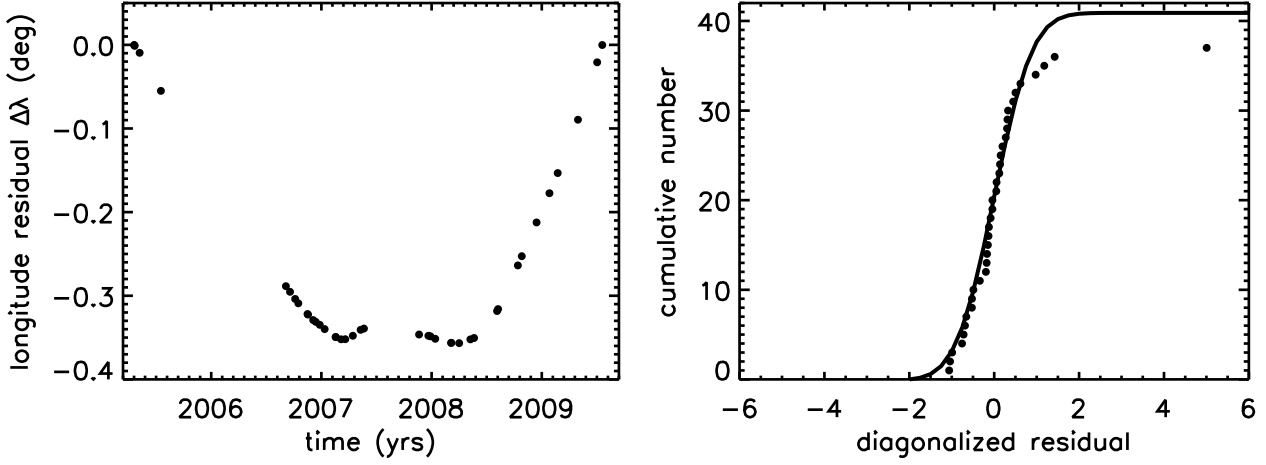


Figure 2. Checking the diagonalization test with a simulated integrated Gaussian random walk. A kick drawn from a Gaussian distribution of width 1 m in semimajor axis is applied every $\delta t = \Omega^{-1} = 8842$ s. The left panel shows the simulated longitude residuals sampled at the Blériot observation times (binned). For display purposes, we subtracted a linear trend to place the first and last data points at zero longitude residual. The right panel shows the results of the diagonalization test. The sorted diagonalized residuals (filled circles) are a reasonable match for Gaussian random variables (solid line). The 4 outliers dropped in calculating \hat{c} all lie outside the range shown in this plot.

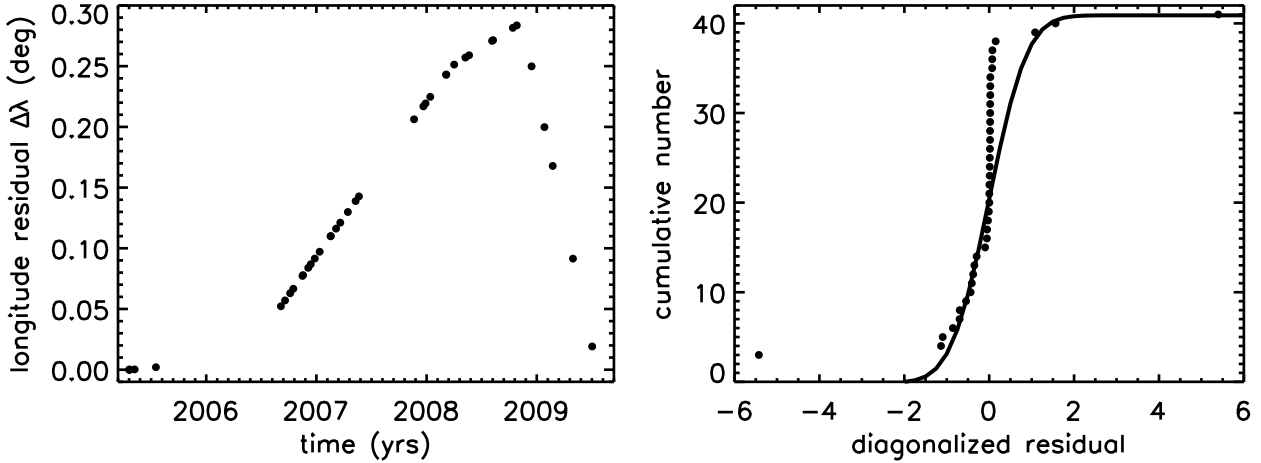


Figure 3. Checking the diagonalization test with a simulated integrated Lévy flight: same as Figure 2 except that here the kick magnitudes $|\delta a|$ have a power-law cumulative distribution $\propto |\delta a|^{-2/5}$. The sorted diagonalized residuals (filled circles in right panel) do not conform to a Gaussian distribution (solid line). In this case, 3 outliers were excluded in the calculation of \hat{c} , and all fall outside the range shown in the right-hand panel.

binned Blériot observation times. We then perform the diagonalization test on the samples. As Figure 3 shows, the diagonalized residuals are distinctly non-Gaussian in shape.

In a world free of measurement uncertainty, we could use \hat{c} to constrain the product of $\delta a/a$ and $\Omega\delta t$ and thus obtain a joint constraint on the moonlet’s diffusivity $D \equiv (\delta a)^2/\delta t$. Unfortunately, we have found by direct experiment that \hat{c} is quite sensitive to measurement uncertainty. For example, randomly altering the longitudes shown in the left panel of Figure 2 by $\sim 2\%$, an amount comparable to the uncertainties reported for the observed Blériot longitudes, gives \hat{c} an order of magnitude larger than that computed using the unaltered longitudes. A similar result is obtained

for the Lévy flight experiment in Figure 3. Fortunately, the shapes of the diagonalized residual distributions still yield the same qualitative answers: with measurement uncertainties included, the simulated integrated Gaussian random walk still passes the diagonalization test, and the simulated integrated Lévy flight still fails the test. Thus we remain confident that, for the parameters of the problem at hand, as long as relative measurement uncertainties remain at the level of a few percent — as they seem to be for the actual data of Blériot — the diagonalized residuals can still be used to give a “yes-or-no” answer to the question of whether the input data are consistent with an integrated Gaussian random walk.

2.3 Blériot

We apply the diagonalization test to Blériot. In mapping a given time t_k to an integer $n = t_k/\delta t$, we take the width δt of each time bin to equal the dynamical time $\Omega^{-1} = 8842$ s, for the physical reason that each encounter between the moonlet and a ring particle which changes the moonlet’s semimajor axis takes a dynamical time to complete (see §3.1). We could take time bins of larger width, but that would reduce the number of points in our input time series. The precise choice of δt is, in any case, not crucial because the random walk is approximately scale invariant: the distribution of $\overrightarrow{\Delta\lambda}$ depends primarily on the combination of δt and δa through the diffusion coefficient $D \equiv (\delta a)^2/\delta t$. To see this, note from Eq. 11 that the covariance matrix Σ of $\overrightarrow{\Delta\lambda}$ satisfies

$$\begin{aligned}\Sigma_{k\ell} &= \left(\frac{3\Omega\delta t\delta a}{2a}\right)^2 \frac{t_k}{6\delta t} \left(1 - \left(\frac{t_k}{\delta t}\right)^2 + 3\frac{t_\ell}{\delta t} + 3\frac{t_k}{\delta t}\frac{t_\ell}{\delta t}\right) \\ &\approx \left(\frac{3\Omega}{2a}\right)^2 D \frac{t_k}{6} (3t_k t_\ell - t_k^2)\end{aligned}$$

for $t_k \leq t_\ell$. Hence, the probability model for $\overrightarrow{\Delta\lambda}$ is, to first order, unaffected by a change in δt , provided that δt is sufficiently small and δa is also changed so as to keep the diffusivity D constant. The same calculation shows that if δt is changed to $h\delta t$ for some constant h , then $\tilde{\Sigma}$ is, to first order, changed to $h^{-3}\tilde{\Sigma}$. Then \tilde{r} and \hat{c} become respectively $h^{3/2}\tilde{r}$ and $h^{3/2}\hat{c}$, so that $\hat{c}^{-1}\tilde{r}$ is, to first order, unchanged. Consequently, the diagonalization test is effectively invariant with respect to a change in the choice of δt .

Many points in Blériot’s published time series are separated by less than $\delta t = \Omega^{-1}$, as multiple images were taken in short succession. The longitudes that fall into the same time bin are averaged into one number. Measurement uncertainties are added in quadrature. Binned this way, there are 41 “independent” longitude measurements, as shown in Figure 4 (left panel).³

The matrix operations in Eq. 12 are applied to the binned longitude residuals $\{\Delta\lambda(t_k)\}$ to compute the diagonalized residuals $\hat{c}^{-1}\{\tilde{r}_k\}$. In this case, 3 outlier values were dropped in the computation of \hat{c} . Figure 4 shows the distribution of diagonalized residuals. It is close to Gaussian; compare with Figures 2 and 3.

We have explored the sensitivity of these results to measurement uncertainties in Blériot’s data. Ten different realizations of Blériot’s longitude time series were generated by randomly selecting points within the error bars shown in the left panel of Figure 4. In all cases, the diagonalized residuals resembled those shown in the right panel of Figure 4.

Recall our experiments in §2.2 with simulated random

walks, where we found that the magnitude of the diagonalized residuals was sensitive to measurement uncertainty; in particular, the (unnormalized) diagonalized residuals were much larger than expected when measurement errors were added to the random walks. Indeed the same effect seems to manifest here with the actual data for Blériot. The \hat{c} value for Blériot is an order of magnitude larger than the \hat{c} value for the simulated integrated Gaussian walk even though their longitude residuals are of comparable magnitudes. Thus we have no reliable estimator of the true value of c , and thus no constraint on the moonlet’s diffusivity D from the results of the diagonalization test alone.

Although we cannot measure the moonlet’s diffusivity from the diagonalization test, we still have the original longitude time series of Blériot, in addition to a smattering of longitude data for other propellers (see Table 1 of T10). Taken at face value, these data indicate that moonlet diffusivities must be such as to generate “typical” longitude deviations of ~ 0.1 – 0.3 deg over timescales of ~ 1 – 2 yr. In the next section, we explain how such random walks can physically arise.

3 STOCHASTIC MIGRATION DUE TO LOCAL FLUCTUATIONS IN SURFACE DENSITY

A moonlet can undergo a Gaussian random walk because of Gaussian fluctuations in the number of particles encountered at Hill sphere separations. The fluctuations of interest to us do not depend on ring self-gravity. Fluctuations still occur because of frequent collisions between ring particles that randomize their positions in the time intervals between encounters with the moonlet. We sketch this process analytically (§3.1), test and calibrate our order-of-magnitude scaling relations with numerical N -body simulations (§3.2), and apply our theory of stochastic migration to Blériot and other propellers (§3.3). Many of the ideas in this section have been treated previously (e.g., Murray-Clay & Chiang 2006; Rein & Papaloizou 2010; Crida et al. 2010), but we present them here afresh for clarity and convenience.

3.1 Analytic Description of Gaussian Stochastic Migration

Consider a moonlet of radius R_{moon} at semimajor axis a , embedded in a ring composed of particles each of radius r and mass m . The moonlet and ring particles are assumed individually to have a bulk density ρ_b . The surface mass density of the ring is Σ , and the local orbital frequency is Ω . Ring particles shear by the moonlet and gravitationally perturb it. Particles inside the moonlet’s orbit tend to kick the moonlet onto a larger orbit, while particles outside the moonlet’s orbit tend to push the moonlet inward.

Random fluctuations in the rate of particles encountered cause the moonlet’s semimajor axis to change stochastically. At radial separations on the order of x between a collection of ring particles and the moonlet, the relative Keplerian shearing velocity is $\sim \Omega x$. The duration of an encounter is $\delta t_{\text{enc}} \sim x/(\Omega x) \sim \Omega^{-1}$, independent of x . The number of particles passing conjunction (to either side of

³ Within some bins, the original longitudes differ by more than their published error bars (see, e.g., the cluster of five points near year 2005.38 in Figure 4b of T10). The published uncertainties are probably underestimated, especially in those cases where longitudes are referenced to ring features such as the Encke gap edge instead of to stars. We have verified with M. Tiscareno (2012, personal communication) that our binning procedure is justified given the quality of the data.

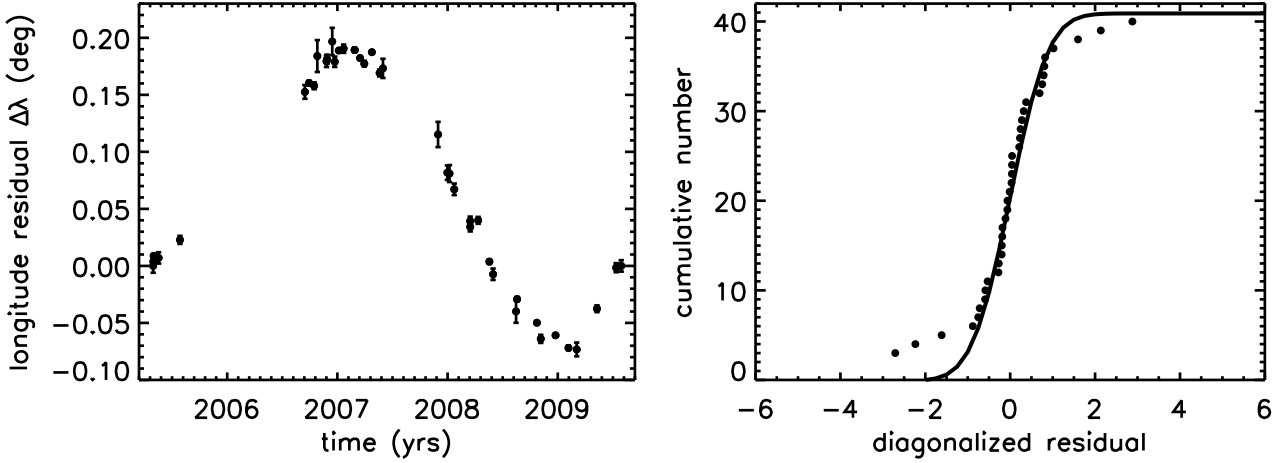


Figure 4. Results of the diagonalization test for Blériot: same as Figure 2 but for the actual data for Blériot rather than for simulation results. The data are binned into 41 points such that the time interval between bins is at least $\Omega^{-1} = 8842$ s long. The diagonalized residuals are reasonably close to Gaussian-distributed; compare with Figures 2 and 3. As in previous figures, the 3 outliers excluded from the calculation of \hat{c} fall outside the range shown in the right panel.

the moonlet’s orbit) per δt_{enc} should follow a Poisson distribution with mean $N_{\text{enc}} \sim \Sigma x^2/m$ and width $\sqrt{N_{\text{enc}}}$.

The randomly varying excess number of particles — lying to either side with equal probability — is responsible for net changes in the moonlet’s semimajor axis. We call the mass of this excess group of particles, tallied every encounter time δt_{enc} , the “fluctuation mass” m_{fluct} . If $N_{\text{enc}} \gg 1$, we can treat m_{fluct} as approximately Gaussian-distributed with mean zero and width $\sim m\sqrt{N_{\text{enc}}}$: positive/negative signs correspond to excess groups of particles passing outside/inside the moonlet’s orbit. An encounter with a fluctuation mass occurs once every δt_{enc} , and each encounter changes the moonlet’s velocity by $\delta v \sim (Gm_{\text{fluct}}/x^2) \times \delta t_{\text{enc}}$, with G the gravitational constant. The largest fluctuations arise from particles within several Hill sphere radii of the moonlet (Murray-Clay & Chiang 2006; Crida et al. 2010): $x \sim R_{\text{Hill}} = a \left(\frac{4\pi}{9} \rho_b R_{\text{moon}}^3 / m_{\text{Saturn}} \right)^{1/3}$. For such encounters, the fractional change in the moonlet’s semimajor axis is of order the fractional change in its velocity: $\delta a/a \sim \delta v/(\Omega a)$, with equal probability of either sign.⁴

Putting all of the above together, we find that every $\delta t_{\text{enc}} \sim \Omega^{-1}$ time, the moonlet randomly walks in semimajor axis by a step of root-mean-square size

$$\begin{aligned} \delta a &\sim \frac{m_{\text{fluct}}}{m_{\text{Saturn}}} \left(\frac{a}{R_{\text{Hill}}} \right)^2 a \\ &\sim 0.15 \left(\frac{300 \text{ m}}{R_{\text{moon}}} \right) \left(\frac{r}{10 \text{ m}} \right)^{3/2} \\ &\quad \cdot \left(\frac{\Sigma}{40 \text{ g/cm}^2} \right)^{1/2} \left(\frac{1 \text{ g/cm}^3}{\rho_b} \right)^{1/6} \text{ m}. \end{aligned} \quad (18)$$

Over the course of the *Cassini* observations analyzed by T10, a propeller-moonlet will random walk in semimajor axis by

an rms distance

$$\Delta a(t) \sim \delta a \sqrt{\Omega t} \sim 10 \left(\frac{300 \text{ m}}{R_{\text{moon}}} \right) \left(\frac{r}{10 \text{ m}} \right)^{3/2} \left(\frac{t}{2 \text{ yr}} \right)^{1/2} \text{ m} \quad (19)$$

where we have used $\Sigma = 40 \text{ g cm}^{-2}$ and $\rho_b = 1 \text{ g cm}^{-3}$. Comparison with Eq. 1 shows that this is of the right order of magnitude to explain the observed non-Keplerian motions of propellers. In the next section we employ N -body simulations to test our scaling relations and measure more accurately the moonlet’s diffusivity. That is, we will revise our crudely estimated coefficients in Eqs. 18 and 19 in accord with the numerical simulations.

3.2 Numerical Simulations of Gaussian Stochastic Migration

We perform shearing box simulations of a moonlet randomly perturbed by nearby ring particles. We use the freely available collisional N -body code **REBOUND** (Rein & Liu 2012) with shear periodic boundary conditions and the symplectic epicycle integrator (SEI, Rein & Tremaine 2011).

The simulations are similar to the test-particle simulations performed by Crida et al. (2010) but include particle-particle and particle-moonlet collisions. Unlike the simulations of Rein & Papaloizou (2010) and Lewis & Stewart (2009), ours do not explicitly include self-gravity. As explained in §1, self-gravity wakes probably make only a small contribution to the observed longitude residuals of propellers as large as Blériot. The mean self-gravitational field does enhance the vertical frequency Ω_z of epicyclic motion (e.g., Wisdom & Tremaine 1988); we mock up this effect in the code by setting $\Omega_z = 3.6\Omega$. All simulations are performed with $\Omega = 1.131 \cdot 10^{-4} \text{ s}^{-1}$ corresponding to a semimajor axis of $a = 130000 \text{ km}$. The timestep was chosen to be $dt = 10^{-3} 2\pi/\Omega$.

Simulation parameters are listed in Table 1. The ring

⁴ This relation holds for $x \sim R_{\text{Hill}}$, but not for $x \gg R_{\text{Hill}}$.

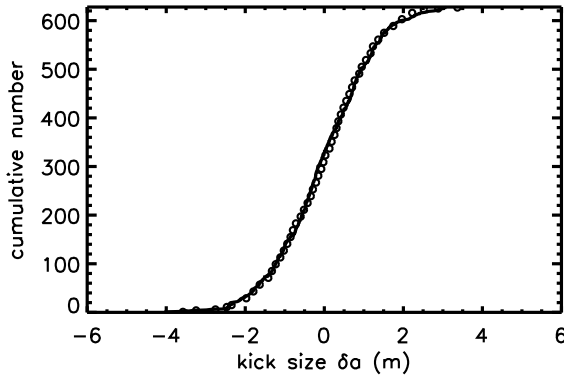


Figure 5. Distribution of kicks (changes in semimajor axis) felt by our simulated 100-m moonlet embedded in a ring with surface density $\Sigma = 40 \text{ g cm}^{-2}$, maximum particle size $r_{\text{max}} = 10 \text{ m}$, minimum particle size $r_{\text{min}} = 2.5 \text{ m}$, and power-law index $q = 3$ for the differential size distribution of particles. Kicks are computed every time interval Ω^{-1} ; their cumulative distribution (solid line) conforms closely to a Gaussian (open circles). The typical kick size, $\delta a \sim 1.5 \text{ m}$, is consistent with our order-of-magnitude estimate in Eq. 18.

particles and moonlet are assumed to have a bulk density $\rho_b = 0.4 \text{ g/cm}^3$. Ring particles are assumed to follow a differential size distribution $dN/dr \propto r^{-q}$ from r_{min} to r_{max} . The slope q is fixed at 3, which places most of the mass in the largest ring particles. Some of our chosen particle size parameters are compatible with occultation and imaging observations (Cuzzi et al. 2009; T10). Others were chosen only to provide a large enough dynamic range to probe how stochasticity scales with the particle radius r .

Ring particles are initialized with zero random velocity (i.e., their initial velocity is determined purely by Keplerian shear). Once a ring particle exits an azimuthal boundary of the simulation domain, it re-enters the domain on the opposite side at a randomized radial location (semimajor axis), with zero random velocity. Thus the number of ring particles N in the box remains constant. The dimensions of the box are L_x , L_y , and L_z in the radial, azimuthal, and vertical directions, respectively. In nearly all cases, $L_x \times L_y$ covers $\sim 27 \times 135$ moonlet Hill radii, while L_z is chosen large enough so that no particle ever reaches a vertical boundary.

Figure 5 shows the distribution of semimajor axis changes or “kicks” δa , evaluated every time interval $\delta t = 1/\Omega$, for simulation 9. The empirical distribution of kicks is close to Gaussian, confirming our physical description of stochastic migration in §3.1. Furthermore, the characteristic value of δa (defined as the 1σ half-width of the Gaussian distribution) is 1.5 m, which agrees to order-of-magnitude with the prediction of Eq. 18 for a 100-m moonlet. In fact, the simulated characteristic value for δa is about 3 times larger than predicted by our back-of-the-envelope estimate. The enhanced fluctuations revealed by the numerical simulations strengthen the case for perturbations from the largest (decameter-sized) ring particles (§3.3) as the main cause of the propellers’ observed non-Keplerian motions. We spec-

ulate that the factor of 3 might arise from two effects in our numerical simulations that are omitted from our simple analysis in §3.1: ring particles on horseshoe orbits, and direct collisions between ring particles and the moonlet (Rein & Papaloizou 2010; see also Murray-Clay & Chiang 2006 who show that encounters with horseshoe librators enhance stochasticity by a factor of order unity).

Figure 6 shows how the moonlet’s longitude residuals evolve in simulation 17, whose parameters are the same as those of simulation 9 but is run for 5 years. In order to avoid impractically long runtimes, simulation 17 uses a smaller box size than simulation 9. However, we expect the results to be insensitive to the change in box size: the most important interactions are with particles passing within $\sim R_{\text{Hill}}$ of the moonlet (§3.1) and the smaller box is still several R_{Hill} in size. We applied the diagonalization test to simulation 17, sampling the longitude residuals at the same set of 41 times that characterize Blériot’s binned data. The diagonalized residuals, shown in Figure 6, verify that the behavior of the simulated moonlet is consistent with that of an integrated Gaussian random walk.

Figure 7 shows the characteristic value of δa versus both particle radius r and moonlet radius R_{moon} . We compute this characteristic value by plotting a cumulative Gaussian distribution against the kicks sorted from smallest to largest, performing a least-squares fit to a line, and varying the width of the Gaussian until the slope of the fitted line is 1. We take the Gaussian width so derived to be the characteristic δa . The scalings expected from Eq. 18 are approximately confirmed. The agreement for r is better than for R_{moon} , but we consider both acceptable. Using our numerical simulations to normalize our analytic scalings, we calibrate Eqs. 18 and 19 into more accurate forms:

$$\delta a \approx 0.5 \left(\frac{300 \text{ m}}{R_{\text{moon}}} \right) \left(\frac{r}{10 \text{ m}} \right)^{3/2} \cdot \left(\frac{\Sigma}{40 \text{ g/cm}^2} \right)^{1/2} \left(\frac{1 \text{ g/cm}^3}{\rho_b} \right)^{1/6} \text{ m} \quad (20)$$

and

$$\Delta a(t) \sim \delta a \sqrt{\Omega t} \approx 30 \left(\frac{300 \text{ m}}{R_{\text{moon}}} \right) \left(\frac{r}{10 \text{ m}} \right)^{3/2} \left(\frac{t}{2 \text{ yr}} \right)^{1/2} \text{ m}. \quad (21)$$

3.3 Implications for Blériot

Observations of Blériot require $\Delta a \simeq 30 \text{ m}$ over a period of ~ 2 years. We can use Eq. 21, which is calibrated using numerical simulations, to estimate how big the surrounding ring particles must be to reproduce these observed parameters.

The radius of Blériot’s moonlet is thought to lie in the range $R_{\text{moon}} = 300\text{--}1200 \text{ m}$ (see Figure 2 of T10). If we adopt $R_{\text{moon}} = 700 \text{ m}$, then a particle size of $r \simeq 18 \text{ m}$ would satisfy the observations assuming a bulk density of 1 g/cm^3 for all bodies. That is, the $1\text{-}\sigma$ excursion in semimajor axis for a 700-m moonlet is $\Delta a \simeq 30 \text{ m}$ over $\Delta t = 2 \text{ yr}$ when $r = 18 \text{ m}$. If the observed $\Delta a \simeq 30 \text{ m}$ actually represents a $2\text{-}\sigma$ excursion, then the required particle size decreases to $r = 11 \text{ m}$.

Sim. Number	R_{moon} (m)	Σ (g/cm ²)	ρ_b (g/cm ³)	r_{min} (m)	r_{max} (m)	q	L_x (m)	L_y (m)	L_z (m)	N	Time (1/ Ω)
1	100	40	0.4	2.5	95	3	3500	17500	1000	19504	540.6
2	100	40	0.4	2.5	85	3	3500	17500	1000	21068	540.6
3	100	40	0.4	2.5	75	3	3500	17500	1000	21992	540.6
4	100	40	0.4	2.5	55	3	3500	17500	1000	23699	540.6
5	100	40	0.4	2.5	45	3	3500	17500	1000	27968	540.6
6	100	40	0.4	2.5	35	3	3500	17500	1000	36662	540.6
7	100	40	0.4	2.5	25	3	3500	17500	1000	51925	540.6
8	100	40	0.4	2.5	15	3	3500	17500	1000	90656	540.6
9	100	40	0.4	2.5	10	3	3500	17500	1000	145912	540.6
10	100	40	0.4	2.5	5	3	3500	17500	1000	350177	540.6
11	100	40	0.4	2.5	2.5	3	3500	17500	1000	935860	540.6
12	50	40	0.4	14.5	15	3	1750	8750	1000	1121	540.6
13	100	40	0.4	14.5	15	3	3500	17500	1000	4390	522.6
14	200	40	0.4	14.5	15	3	7000	35000	1000	17416	540.6
15	400	40	0.4	14.5	15	3	14000	70000	1000	69545	540.6
16	800	40	0.4	14.5	15	3	28000	140000	1000	277980	473.6
17	100	40	0.4	2.5	10	3	1000	2000	1000	4812	20738

Table 1. Parameters of simulations using REBOUND, a shearing box code for colliding particles. The duration of each simulation is given in units of $1/\Omega$. See text for description.

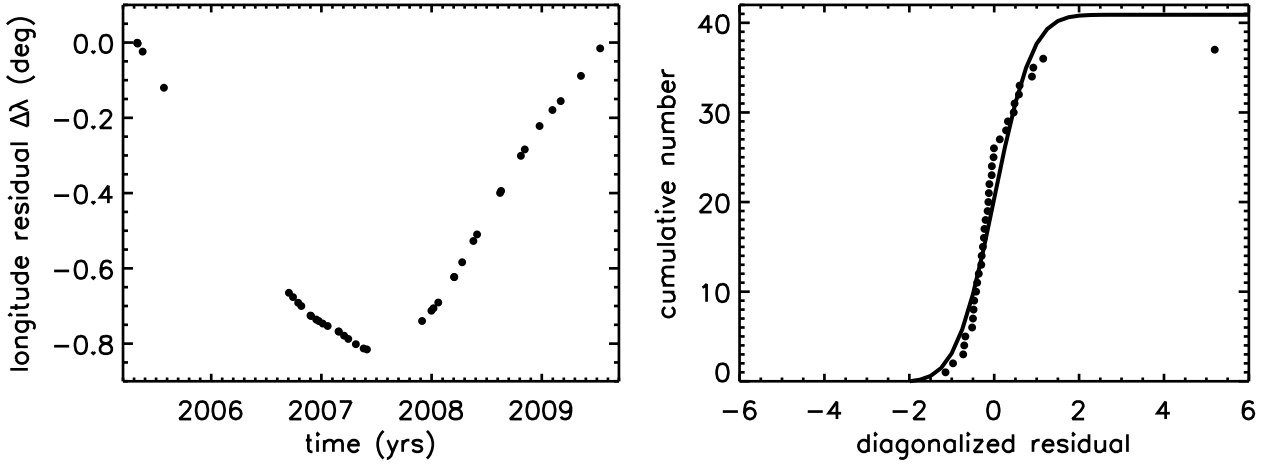


Figure 6. Results of the diagonalization test for simulation 17: same as Figure 2 but for simulation 17 sampled at the 41 binned observation times of Blériot. Here 4 outliers were excluded from the calculation of \hat{c} , and all lie outside the range shown in the right-hand panel. The longitude residuals shown in the left panel are simulation data sampled at times corresponding to the Blériot observation times. The residuals’ distribution is close to Gaussian.

In fact, ground- and space-based occultation data of the outer A ring independently indicate that the bulk of the ring mass resides in particles of size $r = 10\text{--}20$ m (for a summary of what is known about particle size distributions based on occultation analysis, see Cuzzi et al. 2009). For the region just outside the Encke gap which contains Blériot and the other giant propellers, fits to Voyager observations yield a maximum particle size $r_{\text{max}} = 8.9$ m and $q = 3.03$ (Zebker et al. 1985). An analysis of ground-based occultation data gives $r_{\text{max}} = 20$ m and $q = 2.9$ (French & Nicholson 2000). We conclude that stochastic gravitational interactions between propeller moonlets and the largest nearby particles in the outer A ring can readily reproduce longitude residuals like those observed for Blériot.

4 SUMMARY

Whether the migration patterns of propellers arise from a deterministic or random process is not obvious just by looking at their longitude residuals. The difficulty arises because longitude residuals are time-integrated quantities. The time integration smooths out semimajor axis variations that could be noisy, and introduces correlations between data at a given time and all earlier times.

The “diagonalization test” removes correlations introduced by time integration of a Gaussian random process. It tests whether a given time series is compatible with an integrated Gaussian random walk. We have applied the diagonalization test to the longitude time series of the propeller Blériot and found that it passes the test. Blériot’s behavior

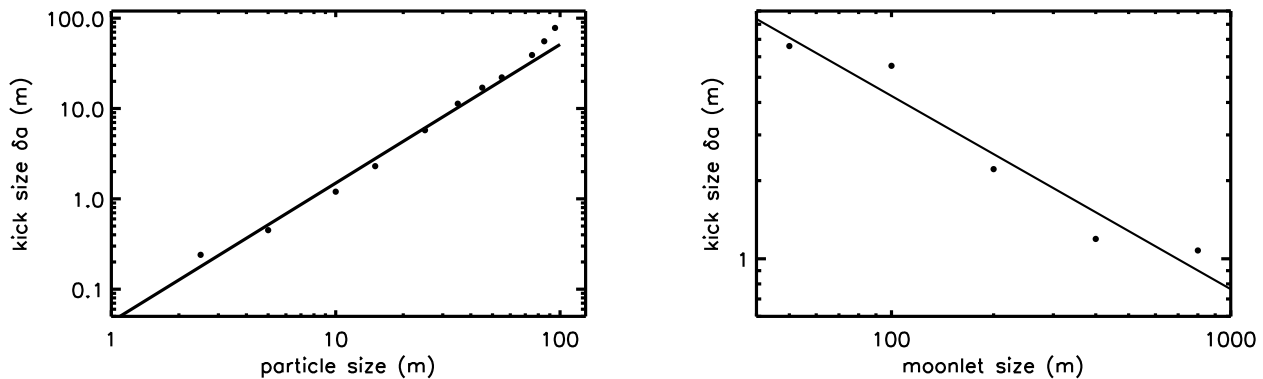


Figure 7. Characteristic δa value, or “kick size”, for simulations 1–11 (left panel) and 12–16 (right panel). Simulations 1–11 show how varying the maximum particle size affects the typical δa . The best-fit power law shown has index 1.47. This agrees well with the predicted slope of 1.5 from Eq. 18. The fit uses only data from simulations 6–11: in simulations 1–5, the largest ring particles are so rare that $N_{\text{enc}} \lesssim 1$. Simulations 12–16 show how varying the moonlet size affects the typical δa . The best-fit power law shown has slope -0.74 ; given the scatter in the data, we consider this acceptable agreement with Eq. 18, which predicts a slope of -1 .

is consistent with that of an integrated Gaussian random walk.

By combining simple analytic scaling relations with numerical N -body simulations, we also showed that moonlets as large as Blériot, having radii of ~ 700 m, could exhibit longitude residuals on the order of 0.1 deg over 2 years, when embedded in a ring of surface density 40 g/cm^2 —provided the bulk of the mass of the ring is contained in particles 10–20 m in radius. Such ring properties are inferred on independent grounds by occultation analysis (Cuzzi et al. 2009). The perturbations exerted by large ring particles on propeller-moonlets are stochastic, caused by Poisson fluctuations in the number of ring particles that shear by the moonlet on Hill sphere scales.

The picture of stochastic migration that we support is similar to that first proposed by Rein & Papaloizou (2010), except that the primary contributors to stochasticity are decameter-sized particles, not self-gravity wakes. We have shown by direct N -body simulation (e.g., Figure 6) that particle size distributions that place most of the ring mass in decameter sizes can reproduce longitude residuals like those observed. As the *Cassini* spacecraft emerges from the ring plane in 2012 and resumes observations of propellers, we look forward to measurements of longitude time series for other propellers in addition to Blériot—and to more accurate protocols for making longitude measurements by improvements to the matrix describing the orientation of the ISS camera with respect to the spacecraft. These new and more accurate data can also be subjected to the diagonalization test, and used to test our prediction that longitude residuals scale with moonlet size as $\Delta\lambda \propto R_{\text{moon}}^{-1}$.

ACKNOWLEDGMENTS

We are grateful to Matt Tiscareno for illuminating conversations about the data published in T10; Scott Tremaine for helpful comments at various stages of the project; Philip Stark for arranging

this cross-talk between astronomy and statistics; and an anonymous referee for a thoughtful and constructive report. MP and EC acknowledge support from NSF grant AST-0909210, NASA Outer Planets Research grant NNX12AJ09G, Berkeley’s Center for Integrative Planetary Science, and Berkeley’s Theoretical Astrophysics Center. HR was supported by the Institute for Advanced Study and NSF grant AST-0807444, and SNE acknowledges support from NSF grant DMS-0907630. Some of this work was begun as part of the International Summer Institute for Modeling in Astrophysics held at the Kavli Institute for Astronomy and Astrophysics in Beijing University. We thank the organizers of this summer program, including Pascale Garaud, Doug Lin, and Shang-Fei Liu for their tireless efforts at fostering collaborations, and are indebted to participants Peng Jiang and Zhao Sun for enlightening conversations.

REFERENCES

- Coles, W., Hobbs, G., Champion, D. J., Manchester, R. N., & Verbiest, J. P. W. 2011, *MNRAS*, 418, 561
- Collins, B. F. & Sari, R. 2006, *AJ*, 132, 1316
- Colwell, J. E., Nicholson, P. D., Tiscareno, M. S., et al. 2009, in *Saturn from Cassini-Huygens*, ed. M. Dougherty, L. Esposito, & T. Krimigis (Heidelberg: Springer), 375–412
- Crida, A., Papaloizou, J. C. B., Rein, H., Charnoz, S., & Salmon, J. 2010, *AJ*, 140, 944
- Cuzzi, J., Clark, R., Filacchione, G., et al. 2009, Ring Particle Composition and Size Distribution, ed. Dougherty, M. K., Esposito, L. W., & Krimigis, S. M., 459–
- French, R. G. & Nicholson, P. D. 2000, *Icarus*, 145, 502
- Goldreich, P. & Tremaine, S. 1982, *ARA&A*, 20, 249
- Lewis, M. C. & Stewart, G. R. 2009, *Icarus*, 199, 387
- Mardia, K. V., Kent, J. T., & Bibby, J. M. 1979, Multivariate analysis (London: Academic Press [Harcourt Brace Jovanovich Publishers]), xv+521, probability and Mathematical Statistics: A Series of Monographs and Textbooks
- Murray-Clay, R. A. & Chiang, E. I. 2006, *ApJ*, 651, 1194
- Pan, M. & Chiang, E. 2010, *ApJ Letters*, 722, L178
- Pan, M. & Chiang, E. 2012, *AJ*, 143, 9
- Rein, H. & Liu, S.-F. 2012, *A&A*, 537, A128

- Rein, H. & Papaloizou, J. C. B. 2010, *A&A*, 524, A22
- Rein, H. & Tremaine, S. 2011, *MNRAS*, 415, 3168
- Salo, H. 1995, *Icarus*, 117, 287
- Seiß, M., Spahn, F., Sremčević, M., & Salo, H. 2005, *Geophys. Res. Lett.*, 32, 11205
- Spahn, F. & Sremčević, M. 2000, *A&A*, 358, 368
- Sremčević, M., Spahn, F., & Duschl, W. J. 2002, *MNRAS*, 337, 1139
- Tiscareno, M. S., Burns, J. A., Hedman, M. M., et al. 2006, *Nature*, 440, 648
- Tiscareno, M. S., Burns, J. A., Sremčević, M., et al. 2010, *ApJ Letters*, 718, L92
- Wisdom, J. & Tremaine, S. 1988, *AJ*, 95, 925
- Zebker, H. A., Marouf, E. A., & Tyler, G. L. 1985, *Icarus*, 64, 531